


Cite this: *RSC Adv.*, 2021, 11, 31219

# *In situ* constructed oxygen-vacancy-rich $\text{MoO}_{3-x}$ /porous $\text{g-C}_3\text{N}_4$ heterojunction for synergistically enhanced photocatalytic $\text{H}_2$ evolution†

Yufeng Pan,<sup>a</sup> Bin Xiong,<sup>a</sup> Zha Li,<sup>b</sup> Yan Wu,<sup>ID</sup><sup>a</sup> Chunjie Yan<sup>ID</sup><sup>a</sup> and Huaibin Song<sup>ID</sup><sup>\*a</sup>

A simple method was developed for enhanced synergistic photocatalytic hydrogen evolution by *in situ* constructing of oxygen-vacancy-rich  $\text{MoO}_{3-x}$ /porous  $\text{g-C}_3\text{N}_4$  heterojunctions. Introduction of a  $\text{MoO}_{3-x}$  precursor ( $\text{Mo(OH)}_6$ ) solution into  $\text{g-C}_3\text{N}_4$  nanosheets helped to form a porous structure, and nano-sized oxygen-vacancy-rich  $\text{MoO}_{3-x}$  *in situ* grew and formed a heterojunction with  $\text{g-C}_3\text{N}_4$ , favorable for charge separation and photocatalytic hydrogen evolution (HER). Optimizing the content of the  $\text{MoO}_{3-x}$  precursor in the composite leads to a maximum photocatalytic  $\text{H}_2$  evolution rate of  $4694.3 \mu\text{mol g}^{-1} \text{h}^{-1}$ , which is approximately 4 times higher of that of pure  $\text{g-C}_3\text{N}_4$  ( $1220.1 \mu\text{mol g}^{-1} \text{h}^{-1}$ ). The presence of oxygen vacancies (OVs) could give rise to electron-rich metal sites. High porosity induced more active sites on the pores' edges. Both synergistically enhanced the photocatalytic HER performance. Our study not only presented a facile method to form nano-sized heterojunctions, but also to introduce more active sites by high porosity and efficient charge separation from OVs.

Received 22nd July 2021  
Accepted 13th September 2021

DOI: 10.1039/d1ra05620d

rsc.li/rsc-advances

## 1. Introduction

Photocatalytic hydrogen evolution (HER) is considered to be one of the most promising ways to alleviate the environment and energy crisis.<sup>1–6</sup> However, exploring highly efficient and environmentally-friendly catalysts remains a challenge for the current photocatalysis field.<sup>7</sup> The efficiency of photocatalytic HER lies in three main aspects: (i) the generation and separation of photo-generated charges, (ii) the migration distance of carriers, and (iii) the oxidation–reduction reaction on the surface of photocatalysts.<sup>8</sup> Various strategies have been proposed to improve the photocatalytic efficiency, with a broad range of photocatalysts.<sup>7</sup>

The prevailing photocatalysts include metal oxides,<sup>9</sup> metal sulfides,<sup>10</sup> metal nitrides,<sup>11</sup> organometallic complexes,<sup>12</sup> and metal-free semiconductors.<sup>13–17</sup> Among the various photocatalysts,  $\text{g-C}_3\text{N}_4$ , a metal-free semiconductor, has attracted extensive attention in photocatalytic HER due to its outstanding characteristics, such as appropriate band edge, environmental friendliness, high thermal and chemical stability, facile fabrication and cost-effectiveness.<sup>18,19</sup> However, the photocatalytic HER efficiency of  $\text{g-C}_3\text{N}_4$  is still far from satisfactory, due to the

low specific surface area, limited active sites and fast recombination rate of photogenerated electron–hole ( $\text{e}^-$ – $\text{h}^+$ ) charges.<sup>20</sup>  $\text{g-C}_3\text{N}_4$  nanosheets were reported previously with better performance than bulk  $\text{g-C}_3\text{N}_4$  with increased surface area, higher photogenerated electron reduction potential, better electron transport capacity and longer lifetime *etc.* Our strategy has designed a more efficient nano-junction based on  $\text{g-C}_3\text{N}_4$  nanosheets.

Based on the review, various strategies have been proposed based on  $\text{g-C}_3\text{N}_4$ , including electronic structure modulation, crystal structure engineering, nanostructure and heterostructure construction.<sup>8,21–25</sup> The construction of  $\text{g-C}_3\text{N}_4$ -based heterojunction can help the separation of charges at the interface, as a variety of  $\text{g-C}_3\text{N}_4$ -based heterojunctions has been reported, such as  $\text{TiO}_2/\text{g-C}_3\text{N}_4$ ,<sup>26,27</sup>  $\text{ZnO}/\text{g-C}_3\text{N}_4$ ,<sup>28,29</sup>  $\text{WO}_3/\text{g-C}_3\text{N}_4$ ,<sup>30</sup>  $\text{WS}_2/\text{g-C}_3\text{N}_4$ ,<sup>31</sup>  $\text{NiO}/\text{g-C}_3\text{N}_4$ ,<sup>32</sup>  $\text{ZnIn}_2\text{S}_4/\text{g-C}_3\text{N}_4$ ,<sup>33</sup>  $\text{Zn}_x\text{Cd}_{1-x}\text{In}_2\text{S}_4/\text{g-C}_3\text{N}_4$ ,<sup>34</sup>  $\text{Bi}_2\text{Se}_3/\text{g-C}_3\text{N}_4$ ,<sup>35</sup>  $\text{MoO}_3/\text{1T-MoS}_2/\text{g-C}_3\text{N}_4$ ,<sup>36</sup> *etc.*  $\text{MoO}_3$  has a large band gap of 3 eV and a high dielectric constant of 6–18, suitable for constructing heterojunction photocatalysis with  $\text{g-C}_3\text{N}_4$ .<sup>37–39</sup> Oxygen-vacancy-rich  $\text{MoO}_{3-x}$  was even more favourable. The synthesis of porous  $\text{g-C}_3\text{N}_4$  and few-layered  $\text{MoO}_3$  has been widely reported, however, the combination of porous  $\text{g-C}_3\text{N}_4$  and oxygen-vacancy-rich  $\text{MoO}_{3-x}$  to construct  $\text{MoO}_{3-x}/\text{g-C}_3\text{N}_4$  photocatalytic system remains a great challenge. The introduction of porous structure in  $\text{g-C}_3\text{N}_4$  usually produces many photocatalytic active sites.<sup>40</sup> Xiao *et al.* introduced a bottom-up method for preparing porous few-layer  $\text{g-C}_3\text{N}_4$  by a sequential molecule self-assembly, alcohol molecules intercalation, thermal-induced exfoliation and polycondensation process.<sup>40</sup> Moreover, conventional silicon dioxide ( $\text{SiO}_2$ )

<sup>a</sup>Engineering Research Center of Nano-Geomaterials of Ministry of Education, Faculty of Materials Science and Chemistry, China University of Geosciences, Wuhan 430074, China. E-mail: songhb@cug.edu.cn

<sup>b</sup>Wuhan National Laboratory for Optoelectronics, Huazhong University of Science and Technology, Wuhan, Hubei, 430074, P. R. China

† Electronic supplementary information (ESI) available. See DOI: 10.1039/d1ra05620d



template or ammonium bicarbonate ( $\text{NH}_4\text{HCO}_3$ ) has also been used as pore forming agent to prepare porous  $\text{g-C}_3\text{N}_4$  in the process of polycondensation.<sup>41,42</sup> For the construction of oxygen vacancies, metal oxides with oxygen vacancies are usually obtained by using hydrogen thermal treatment,<sup>43</sup> high energy particle bombardment,<sup>44</sup> and heating metal oxides under vacuum or oxygen depleted conditions.<sup>45</sup> Although these methods have their own advantages, they are inevitably limited by high-energy input and complex post-processing. According to the literature, there are electrostatic composite and *in situ* construction method.<sup>41,46</sup> The former is simple to implement, but it is greatly affected by the pH of photocatalytic reaction. Therefore, it is urgent to develop a new method to integrate porous structure and oxygen vacancy into a heterojunction system.

Herein, we propose a salt assisted *in situ* growth method to construct nano-sized oxygen-vacancy-rich  $\text{MoO}_{3-x}$ /porous  $\text{g-C}_3\text{N}_4$  heterojunction. The introduction of  $\text{MoO}_{3-x}$  precursor ( $\text{Mo}(\text{OH})_6$ ) into  $\text{g-C}_3\text{N}_4$  not only helps to prepare porous nanosheets, but also *in situ* grown oxygen-vacancy-rich  $\text{MoO}_{3-x}$  can form an atomic-scale compact heterointerface with  $\text{g-C}_3\text{N}_4$ . In addition, the heterojunction between  $\text{MoO}_{3-x}$  and  $\text{g-C}_3\text{N}_4$  was established, which synergistically improved photocatalytic HER performance, including higher charge separation efficiency, shorter charge transport path, and more catalytic active sites. By HR-TEM, HAADF-STEM and AFM, the morphology of the nanosized  $\text{MoO}_{3-x}$ /porous  $\text{g-C}_3\text{N}_4$  heterojunction was confirmed. XPS proved the oxygen-vacancy in  $\text{MoO}_{3-x}$ . As a result, the optimized  $\text{MoO}_{3-x}$ / $\text{g-C}_3\text{N}_4$  heterojunction produces  $\text{H}_2$  at  $4694.3 \mu\text{mol g}^{-1} \text{h}^{-1}$ , approximately 4 times higher of that of pure  $\text{g-C}_3\text{N}_4$  ( $1220.1 \mu\text{mol g}^{-1} \text{h}^{-1}$ ). Our strategy can be universal for constructing diverse heterojunction with OVs and porous characteristics.

## 2. Experimental sections

### 2.1. Materials and reagents

All chemical reagents and materials were purchased and used without further purification. Molybdenum powder ( $\text{Mo}$ , 98%), urea ( $(\text{NH}_2)_2\text{CO}$ ,  $\geq 98\%$ ) were purchased from Sigma. Sodium chloride ( $\text{NaCl}$ , AR), absolute ethanol ( $\text{CH}_3\text{CH}_2\text{OH}$ , AR), and triethanolamine (TEOA, AR) were purchased from Sinopharm Chemical Reagent Co., Ltd. All chemicals were analytical grade and used without further purification.

### 2.2. Preparation of $\text{g-C}_3\text{N}_4$

$\text{g-C}_3\text{N}_4$  was synthesized by thermal condensation of urea directly. In detail, 10 g urea powder was placed in an alumina crucible and heated to  $550^\circ\text{C}$  for 2 h in static air with a heating rate of  $5^\circ\text{C min}^{-1}$ . The resulting yellow agglomerates were then collected and milled into powder for further synthesis and measurements.

### 2.3. Preparation of $\text{Mo}(\text{OH})_6$ precursor

Typically, 0.1 g molybdenum ( $\text{Mo}$ ) powder was dispersed in 10 mL ethanol with stirring for several minutes. Then 0.35 mL

$\text{H}_2\text{O}_2$  (30%) solution was added into the  $\text{Mo}$  power suspension solution. After 18 h, the  $\text{Mo}$  oxide solution turned from grey to yellow and finally turned to blue.

### 2.4. Preparation of $\text{MoO}_3$

The 10 mL  $\text{Mo}(\text{OH})_6$  precursor was dried in a  $60^\circ\text{C}$  vacuum oven for 30 min, then transferred to a tubular furnace and calcined at  $400^\circ\text{C}$  for 2 h ( $5^\circ\text{C min}^{-1}$ , under nitrogen condition).

### 2.5. Preparation of $\text{MoO}_{3-x}$

The  $\text{Mo}(\text{OH})_6$  precursor was added into a certain amount of  $\text{NaCl}$ , stirred well, and dried on the heating mantle at  $80^\circ\text{C}$ . Then, transferred to a quartz tube furnace, to anneal for 2 h at  $280^\circ\text{C}$  ( $5^\circ\text{C min}^{-1}$ , under nitrogen condition). The sample was dissolved in deionized water, and then filtered, washed and dried to obtain solid powder.

### 2.6. Preparation of $\text{MoO}_{3-x}$ /porous $\text{g-C}_3\text{N}_4$ nanosheets

A typical fabrication process as follows: 50 mg  $\text{g-C}_3\text{N}_4$  was dissolved in 200 mL of anhydrous ethanol and dispersed it evenly by ultrasonic treatment. 200 g  $\text{NaCl}$  prepared beforehand was added to the solution, followed by stirring, and the ethanol was removed by placing it on a heating mantle at  $80^\circ\text{C}$ , the obtained sample was annealed at  $300^\circ\text{C}$  for 2 h in a quartz tube furnace ( $5^\circ\text{C min}^{-1}$ , under nitrogen condition). The  $\text{Mo}(\text{OH})_6$  precursor was added into the above  $\text{g-C}_3\text{N}_4/\text{NaCl}$  mixture, stirred well, and dried on the heating table at  $80^\circ\text{C}$ . The dried powder was transferred to a quartz tube furnace, to anneal for 2 h at  $280^\circ\text{C}$  ( $5^\circ\text{C min}^{-1}$ , under nitrogen condition). The obtained sample was dissolved in deionized water, filtered, washed and dried to obtain solid powder. 1%, 5%, 10%, 50%  $\text{MoO}_{3-x}/\text{g-C}_3\text{N}_4$  samples were prepared by adjusting the mass ratio of  $\text{Mo}$  powder to  $\text{g-C}_3\text{N}_4$ .  $\text{NaCl}$  acts as a removable template, provides a place for the construction of heterojunction *in situ*, and plays a good role in dispersing  $\text{g-C}_3\text{N}_4$  precursor, so that  $\text{Mo}(\text{OH})_6$  can better contact with  $\text{g-C}_3\text{N}_4$ . As an antisolvent, ethanol does not dissolve  $\text{NaCl}$  and can be quickly removed from the system under  $80^\circ\text{C}$  heating, so it acts as a medium for mixing the two materials.

### 2.7. Characterization

The phase structures of samples were recorded by X-ray powder diffraction (XRD, BrokerAXS Germany). Chemical state analysis was performed by using X-ray photoelectron spectroscopy (XPS, ESCALab 250). FTIR spectrometer (Nicolet iS50) was applied to investigate the functional groups and chemical structure of samples. Scanning electron microscope (SEM, HITACHI SU8010 Hitachi Japan), transmission electron microscope (TEM, Tecnai G20) and atomic force microscope (AFM, BRUKER MultiMode 8) were conducted to confirm the morphology and thickness of samples. Ultraviolet-visible (UV-vis) spectrophotometer (Shimadzu instruments Ltd., Suzhou, UV-2600) and Spectrofluorometer (Edinburgh Instruments Ltd., FS5) measurements were performed to study optical properties of samples. Photocurrent response, EIS Nyquist plots and Mott-Schottky measurements



were conducted to comprehend electrochemical properties with the help of CHI 760E electrochemical system (Chenhua, Shanghai, China).

## 2.8. Photoelectrochemical measurement

Photoelectrochemical experiments were carried out on the CHI 760E electrochemical workstation using a traditional three-electrode system. The Ag/AgCl electrode was used as the reference electrode, Pt electrode was used as the counter electrode, and photocatalyst/ITO was used as working electrode. The detailed preparation of working electrode is as follows: firstly, 10 mg catalyst was dispersed in 2 mL DI water, followed by another ultra-sonication for half an hour to form a uniform suspension. Secondly, the suspension was dropped onto the surface of the ITO glass. Finally, the ITO glass was placed under an infrared lamp for drying. 0.1 mol L<sup>-1</sup> sodium sulfate solution and a 300 W xenon lamp were used as electrolyte solution and light source respectively, in the photocurrent responses and electrochemical impedance spectra experiments. In Mott-Schottky measurement, the frequency is 1000 Hz, the potential range is -1 to 1 V, and the electrolyte solution is 0.5 mol L<sup>-1</sup> sodium sulfate solution.

## 2.9. Photocatalytic H<sub>2</sub> evolution test

The photocatalytic H<sub>2</sub> evolution experiments were carried out in a 200 mL Pyrex reaction cell connected to a glass closed gas circulation system with vacuum (Labsolar-III (AG), Perfectlight Technology Co. Ltd, Beijing, P. R. China). In a photocatalytic reaction, 50 mg as-prepared photocatalyst powder was suspended in a glass cylindrical reactor, then, added to 90 mL deionized water, and stirred for a while. 10 mL triethanolamine (TEOA) was added in the above suspension as a sacrificial agent. The photocatalytic reaction was performed using a 300 W xenon lamp ( $\lambda = 320\text{--}780$  nm). Before irradiation, the whole system maintains a vacuum to avoid contact with air. H<sub>2</sub>PtCl<sub>6</sub> aqueous solution was added as the precursor for the co-catalyst Pt, which was *in situ* photo-reduced during the photocatalytic reaction (2 wt% Pt). The amount of H<sub>2</sub> produced during the photocatalytic reaction was determined by a gas chromatography (Techcomp, GC7900) (TCD detector, 5 Å molecular sieve column) for every one hour.

# 3. Results and discussion

## 3.1. Synthesis of nano-sized oxygen-vacancy-rich MoO<sub>3-x</sub>/porous g-C<sub>3</sub>N<sub>4</sub> heterojunction by salt assisted *in situ* growth method

We schematically illustrated the method in Fig. 1: firstly, g-C<sub>3</sub>N<sub>4</sub> nanosheets were synthesized as the method reported and dispersed in anhydrous ethanol by ultrasonication, followed by adding NaCl powder. After the removal of ethanol by annealing at 80 °C, g-C<sub>3</sub>N<sub>4</sub> nanosheets/NaCl was obtained (step 1). Secondly, the ethanol solution of Mo(OH)<sub>6</sub> as precursor was mixed with the prepared g-C<sub>3</sub>N<sub>4</sub> nanosheets/NaCl, annealing at 280 °C in a CVD furnace to obtain MoO<sub>3-x</sub>/g-C<sub>3</sub>N<sub>4</sub>/NaCl (step 2). Washing with deionized water several times to remove NaCl, the

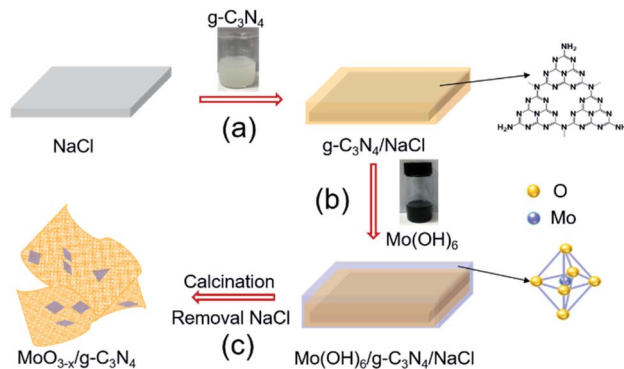


Fig. 1 Schematic diagram of the fabrication processes of oxygen-vacancy-rich MoO<sub>3-x</sub>/porous g-C<sub>3</sub>N<sub>4</sub> heterojunction.

MoO<sub>3-x</sub>/g-C<sub>3</sub>N<sub>4</sub> heterojunction material was obtained (step 3). In addition, by changing the mass ratio of Mo powder to g-C<sub>3</sub>N<sub>4</sub> (1%, 5%, 10%, and 50%), MoO<sub>3-x</sub>/g-C<sub>3</sub>N<sub>4</sub> samples with different Mo percentage were also prepared. The amorphous structure of prepared MoO<sub>3-x</sub>/g-C<sub>3</sub>N<sub>4</sub> nanosheets was confirmed by X-ray diffraction (XRD) analysis as shown in Fig. S1.† Fig. S2† shows the XRD pattern of pure  $\alpha$ -MoO<sub>3</sub> fabricated from Mo(OH)<sub>6</sub> precursor.

## 3.2. Morphological analysis

HAADF-STEM and TEM images revealed the abundant nano-sized pores in nanosheets with tens of nanometers diameter (Fig. 2a and b), consistent with SEM observation (Fig. S3†). MoO<sub>3-x</sub> nanocrystals assembled on the surface of g-C<sub>3</sub>N<sub>4</sub> nanosheets (Fig. 2c and S4†). For further confirmation, EDX elemental mapping of 5% MoO<sub>3-x</sub>/g-C<sub>3</sub>N<sub>4</sub> nanosheets indicated C, N, O, Mo elements distribution in the heterojunction (Fig. 2d–g). Atomic force microscopy (AFM) images showed the thicknesses of 5% MoO<sub>3-x</sub>/g-C<sub>3</sub>N<sub>4</sub> heterojunction around 3–5 nm and pore diameter around tens of nanometers, consistent with (Fig. 2h and S5†). Thus, the microscopic morphology of MoO<sub>3-x</sub>/porous g-C<sub>3</sub>N<sub>4</sub> heterojunction has been confirmed.

## 3.3. The formation of porous g-C<sub>3</sub>N<sub>4</sub> nanosheets

FT-IR was applied to analyse the chemical structures of g-C<sub>3</sub>N<sub>4</sub> nanosheets and 5% MoO<sub>3-x</sub>/g-C<sub>3</sub>N<sub>4</sub> (Fig. 3a). A new vibration band at 2178 cm<sup>-1</sup> in MoO<sub>3-x</sub>/g-C<sub>3</sub>N<sub>4</sub> nanosheets, attributed to C≡N bond, indicated the deprotonation of the amino group (-NH<sub>2</sub>) in g-C<sub>3</sub>N<sub>4</sub> nanosheets.<sup>8</sup> On the other side, NH<sub>3</sub> was released in the deprotonation process, and led to the formation of pores.

To further investigate the chemical states and elemental composition of the samples, XPS and elemental analysis measurements were performed, respectively. As shown Fig. 3b, the XPS spectrum of 5% MoO<sub>3-x</sub>/g-C<sub>3</sub>N<sub>4</sub> nanosheets exhibited C 1s and N 1s signals at the position same as that of g-C<sub>3</sub>N<sub>4</sub> nanosheets. In Fig. 3c, the C 1s peak of g-C<sub>3</sub>N<sub>4</sub> was fitted into two peaks at 284.8, and 288.0 eV, assigned to graphitic C–C, and sp<sup>2</sup>-hybridized carbon in N containing aromatic ring (N–C=N), respectively.<sup>47</sup> The C 1s peak of MoO<sub>3-x</sub>/g-C<sub>3</sub>N<sub>4</sub> (5%) nanosheets slightly shifted from 288.0 eV to 288.2 eV, attributed to the





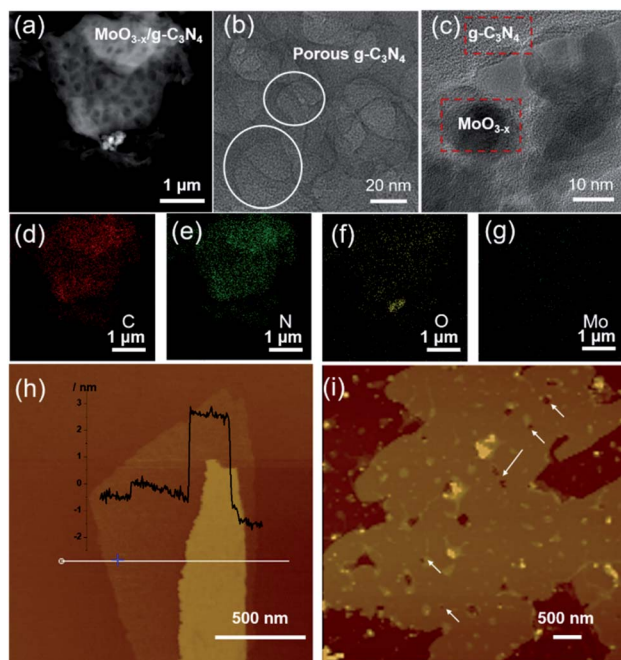


Fig. 2 (a) HAADF-STEM image. (b and c) TEM images. (d–g) EDX elemental maps of  $\text{MoO}_{3-x}/\text{porous g-C}_3\text{N}_4$  heterojunction (C, N, O, Mo). (h) AFM images of BCN and (i)  $\text{MoO}_{3-x}/\text{porous g-C}_3\text{N}_4$  heterojunction.

interaction between  $-\text{NH}_2$  and  $\text{HO-Mo}(\text{OH})_5$ .<sup>8</sup> In Fig. 3d, the N 1s peak for  $\text{g-C}_3\text{N}_4$  could be deconvoluted into four peaks at 398.7, 399.9, 401.0 and 404.4 eV, attributed to the  $\text{sp}^2$ -bonded N in the tri-s-triazine units ( $\text{C}=\text{N}-\text{C}$ ), bridging nitrogen atoms in  $\text{N}(\text{C})_3$ , nitrogen atoms bonded with hydrogen atoms ( $-\text{NH}_x$ )

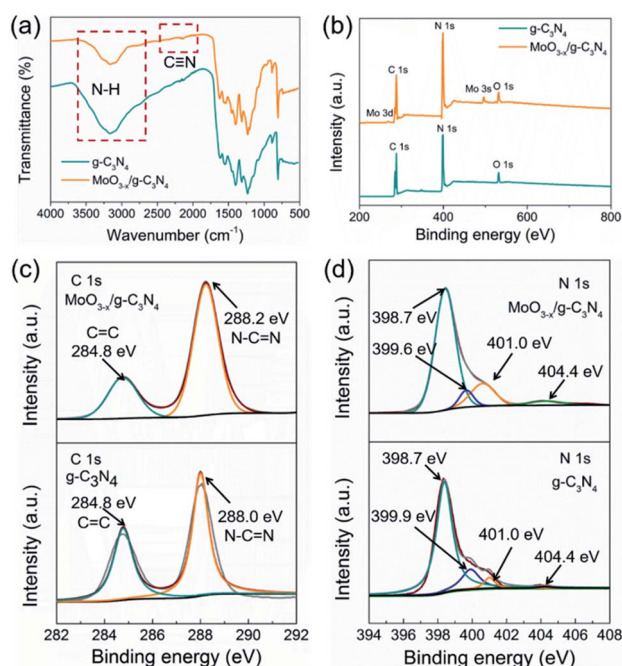


Fig. 3 (a) FTIR spectrum, (b) XPS survey spectra, (c) C 1s XPS profiles and (d) N 1s XPS profiles of  $\text{g-C}_3\text{N}_4$  and  $\text{MoO}_{3-x}/\text{g-C}_3\text{N}_4$  (5%) samples.

and the charging effects, respectively.<sup>47</sup> Compared with  $\text{g-C}_3\text{N}_4$  nanosheets,  $\text{MoO}_{3-x}/\text{g-C}_3\text{N}_4$  (5%) nanosheets showed obvious shift of  $\text{N}(\text{C})_3$  peaks (from 399.9 eV to 399.6 eV), suggesting cyano-groups and consistent with the FTIR results.<sup>48</sup> In addition, the introduction of N defects can be supported by elemental analysis measurements as showed in Table S1,<sup>†</sup> supporting  $\text{NH}_3$  releasing. The N/C atomic ratio for  $\text{g-C}_3\text{N}_4$  is 1.32, close to the ideal  $\text{g-C}_3\text{N}_4$  composition ( $\text{N/C} = 1.33$ ),<sup>49</sup> while the N/C atomic ratios for  $\text{MoO}_{3-x}/\text{g-C}_3\text{N}_4$  (5%) decrease to 1.02, suggesting the loss of lattice nitrogen in  $\text{MoO}_{3-x}/\text{g-C}_3\text{N}_4$  (5%) due to the production of  $\text{NH}_3$ .

### 3.4. The formation of oxygen vacancies on $\text{MoO}_{3-x}$

As a reference, we synthesized  $\text{MoO}_3$  by the reported method. We compared the XPS spectra of the  $\text{MoO}_3$  and 5%  $\text{MoO}_{3-x}/\text{g-C}_3\text{N}_4$  in Fig. 4a and b. For  $\text{MoO}_3$ , the O 1s peaks at 530.5, 532.2, and 533.0 eV, are due to  $\text{Mo-O}$ , oxygen vacancy, and  $-\text{OH}$ , respectively.<sup>50</sup> For  $\text{MoO}_{3-x}/\text{g-C}_3\text{N}_4$  (5%) nanosheets, the O 1s peaks from  $\text{Mo-O}$  and  $-\text{OH}$  positively shifted 0.6 and 1.6 eV, respectively, attributed to the interaction between the  $-\text{OH}$  of  $\text{Mo}(\text{OH})_6$  and the  $-\text{NH}_2$  of  $\text{g-C}_3\text{N}_4$ . In order to further obtain more details information of oxygen vacancy, the ratios of different O species of  $\text{MoO}_3$  and  $\text{MoO}_{3-x}/\text{g-C}_3\text{N}_4$  (5%) calculated by XPS, the analysis results are shown in Tables S2 and S3.<sup>†</sup> The concentration of oxygen vacancy increased from 21.84% to 48.67% in  $\text{MoO}_3$  and  $\text{MoO}_{3-x}/\text{g-C}_3\text{N}_4$  (5%), respectively. By the O 1s spectra comparison, the ratio of  $\text{Mo-O}$  decreases and the ratio of  $-\text{OH}$  increases, suggesting the unsaturation of Mo coordination. In  $\text{MoO}_{3-x}/\text{g-C}_3\text{N}_4$  (5%) composite, the broadened doublets at 231.7 and 234.9 eV are ascribed to the electron binding energies of the Mo 3d<sub>3/2</sub> and Mo 3d<sub>5/2</sub> of  $\text{Mo}^{5+}$  (Fig. 3b). The existence of the  $\text{Mo}^{5+}$  may come from the oxygen vacancies and unsaturated coordination of Mo.<sup>51,52</sup>

### 3.5. Photocatalytic $\text{H}_2$ evolution

Fig. 5a exhibits HER rates of the as-prepared samples all with 2 wt% Pt as co-catalyst and TEOA as hole-sacrificial agent. The 5%  $\text{MoO}_{3-x}/\text{g-C}_3\text{N}_4$  heterojunction exhibits the highest HER activity as the optimized condition and lower or higher  $\text{MoO}_{3-x}$  percentage induced less HER activity. With the further

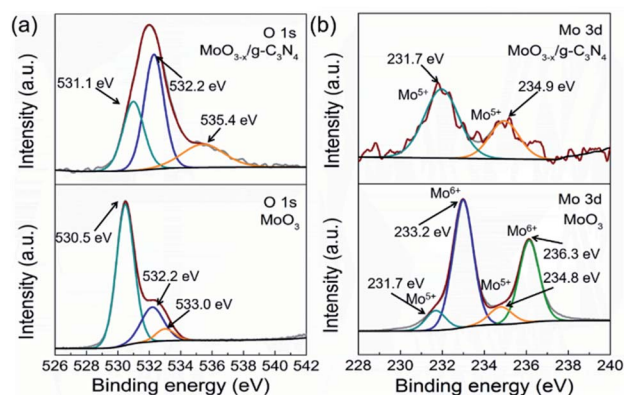


Fig. 4 (a) O 1s XPS and Mo 3d XPS profiles (b) of  $\alpha\text{-MoO}_3$  and  $\text{MoO}_{3-x}/\text{g-C}_3\text{N}_4$  (5%) nanosheets.

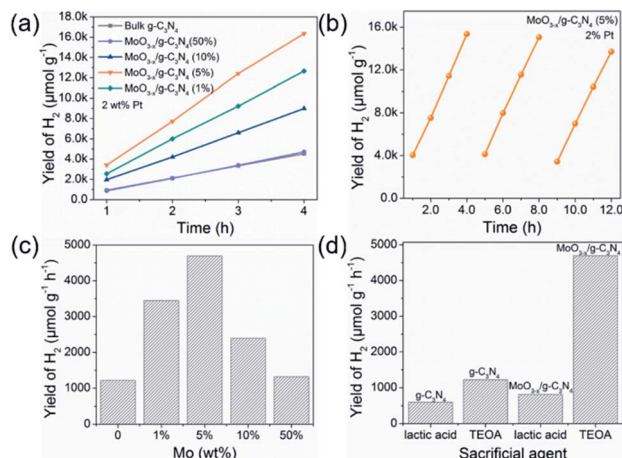


Fig. 5 Photocatalytic  $\text{H}_2$  evolution performance and stability test. (a) The photocatalytic  $\text{H}_2$  evolution of  $\text{MoO}_{3-x}/\text{g-C}_3\text{N}_4$  samples with 2 wt% Pt as co-catalyst. (b) Photocatalytic cycle stability test of 5%  $\text{MoO}_{3-x}/\text{g-C}_3\text{N}_4$  with 2 wt% Pt as co-catalyst. (c) Optimum photocatalytic  $\text{H}_2$  evolution efficiency of  $\text{MoO}_{3-x}/\text{g-C}_3\text{N}_4$  photocatalysts with different contents of  $\text{MoO}_{3-x}$ . (d) The photocatalytic hydrogen evolution performance for  $\text{g-C}_3\text{N}_4$  and 5%  $\text{MoO}_{3-x}/\text{g-C}_3\text{N}_4$  with 2 wt% Pt as co-catalyst in different sacrificial agent systems (lactic acid and TEOA).

increasing  $\text{MoO}_{3-x}$ , excess  $\text{MoO}_{3-x}$  has a tendency to self-aggregate, reducing effective interfacial area between  $\text{MoO}_{3-x}$  and  $\text{g-C}_3\text{N}_4$  and the active sites. So, the overmounted  $\text{MoO}_{3-x}$  led to lower performance. Fig. 5b shows that the high HER stability of 5%  $\text{MoO}_{3-x}/\text{g-C}_3\text{N}_4$  nanosheets, with no obvious decrease during 3 cycles. Fig. 5c compared the HER rate with different percentage of  $\text{MoO}_{3-x}$  in  $\text{MoO}_{3-x}/\text{g-C}_3\text{N}_4$  nanosheets. The 5%  $\text{MoO}_{3-x}/\text{g-C}_3\text{N}_4$  nanosheets exhibits the highest HER rate ( $4694.3 \mu\text{mol g}^{-1} \text{h}^{-1}$ ), about 4 times higher than pure  $\text{g-C}_3\text{N}_4$  ( $1220.1 \mu\text{mol g}^{-1} \text{h}^{-1}$ ). Fig. 5d compared the HER rates of the pure  $\text{g-C}_3\text{N}_4$  and 5%  $\text{MoO}_{3-x}/\text{g-C}_3\text{N}_4$  nanosheets using lactic acid and TEOA as hole-sacrificial agents, respectively.  $\text{MoO}_{3-x}/\text{g-C}_3\text{N}_4$  (5%) nanosheets exhibited higher HER rates in both systems of lactic acid and TEOA as hole-sacrificial agents. Photocatalytic hydrogen evolution rates of  $\text{g-C}_3\text{N}_4$ , 5%  $\text{MoO}_3/\text{g-C}_3\text{N}_4$  and 5%  $\text{MoO}_{3-x}/\text{g-C}_3\text{N}_4$  as shown in Fig. S6.† 5%  $\text{MoO}_{3-x}/\text{g-C}_3\text{N}_4$  showed the best HER performance, which further proved the promoting effect of OV in  $\text{MoO}_{3-x}/\text{g-C}_3\text{N}_4$  photocatalyst on HER. We also compared the HER performance of similar photocatalysts reported in some recent references as shown in Table S4.†

### 3.6. The electronic structure and photocatalytic mechanism

The optical absorption properties and band gap of the heterojunction were studied by UV-vis absorption spectroscopy. The  $\text{g-C}_3\text{N}_4$  shows an absorption edge of approximately 435 nm (Fig. 6a), consistent with the ref. 53. The 5%  $\text{MoO}_{3-x}/\text{g-C}_3\text{N}_4$  heterojunction exhibits a red-shift of absorption edge, given to the interfacial charge transfer (Fig. 6a). UV-vis absorption spectra of  $\text{g-C}_3\text{N}_4$  and  $\text{MoO}_{3-x}$  is shown in Fig. S7,† the illustrations are their corresponding Tauc's plot. In Fig. 6b, the pure

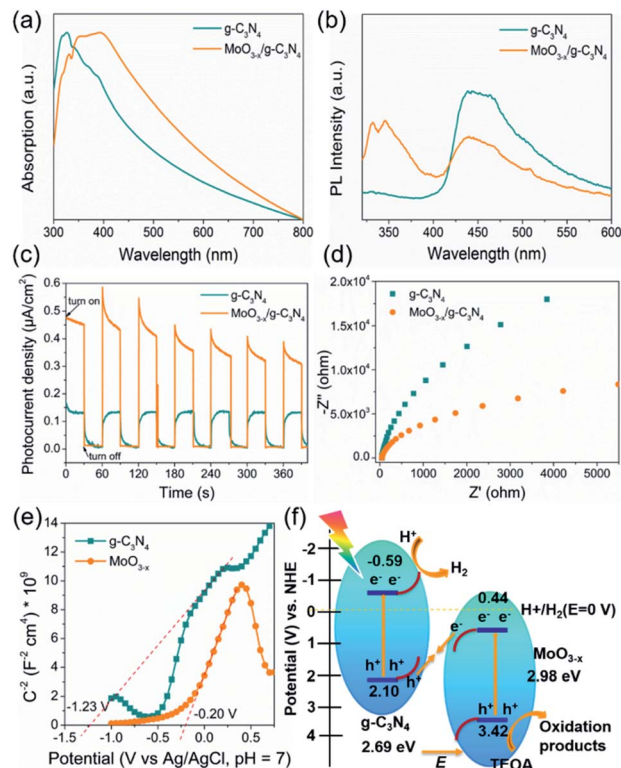


Fig. 6 (a) UV-vis spectra of  $\text{g-C}_3\text{N}_4$  and 5%  $\text{MoO}_{3-x}/\text{g-C}_3\text{N}_4$ . (b) PL emission spectra of  $\text{g-C}_3\text{N}_4$  and 5%  $\text{MoO}_{3-x}/\text{g-C}_3\text{N}_4$ . (c) The transient photocurrent responses under dark and irradiated conditions. (d) The electrochemical impedance spectra of  $\text{g-C}_3\text{N}_4$  and 5%  $\text{MoO}_{3-x}/\text{g-C}_3\text{N}_4$  photocathodes under light. (e) Mott-Schottky plots of  $\text{g-C}_3\text{N}_4$  and  $\text{MoO}_{3-x}$ . (f) The photocatalytic  $\text{H}_2$  evolution mechanism of the  $\text{MoO}_{3-x}/\text{g-C}_3\text{N}_4$  system under light irradiation ( $\lambda = 320\text{--}780 \text{ nm}$ ).

$\text{g-C}_3\text{N}_4$  nanosheets in ethanol exhibited a strong PL peak at 450 nm, while 5%  $\text{MoO}_{3-x}/\text{g-C}_3\text{N}_4$  nanosheets with the same concentration of  $\text{g-C}_3\text{N}_4$  nanosheets in ethanol showed much smaller PL peak at 450 nm. The PL peak at 350 nm was attributed to  $\text{MoO}_{3-x}$  (excitation wavelength: 300 nm). These results suggest that, in the heterojunction, the  $\text{MoO}_{3-x}$  absorbed the excitation energy and transferred some part to  $\text{g-C}_3\text{N}_4$ . In Fig. 6c, the 5%  $\text{MoO}_{3-x}/\text{g-C}_3\text{N}_4$  exhibit higher photocurrent density than  $\text{g-C}_3\text{N}_4$ . Compared with pure  $\text{g-C}_3\text{N}_4$ , 5%  $\text{MoO}_{3-x}/\text{g-C}_3\text{N}_4$  nanosheets have stronger photocurrent density as well as smaller arc radius (Fig. 6d), leading to lower resistance and favourable for charge separation. The corresponding optical band-gaps ( $E_g$ ) were calculated to be 2.69 eV for  $\text{g-C}_3\text{N}_4$  and 2.98 eV for  $\text{MoO}_{3-x}$  (Fig. S7a and b†). In Mott-Schottky plots (Fig. 6e), the extrapolated conduction band edge ( $E_{CB}$ ) positions of  $\text{g-C}_3\text{N}_4$  and  $\text{MoO}_{3-x}$  are  $-1.23$  and  $-0.20 \text{ V}$  (vs.  $\text{Ag}/\text{AgCl}$ ,  $\text{pH} = 7$ ) or  $-0.59$  and  $+0.44 \text{ V}$  (vs.  $\text{NHE}$ ,  $\text{pH} = 0$ ), respectively. Regarding  $E_g$  of  $\text{g-C}_3\text{N}_4$  (2.69 eV) and  $\text{MoO}_{3-x}$  (2.98 eV) nanosheets, the valence band energy ( $E_{VB}$ ) was calculated as 2.10 and 3.42 eV (vs.  $\text{NHE}$ ,  $\text{pH} = 0$ ) as shown in Fig. 6f. According to the step-scheme photocatalytic system,<sup>30</sup> the  $\text{e}^-$  on the CB of  $\text{MoO}_{3-x}$  would recombine with the  $\text{h}^+$  of VB  $\text{g-C}_3\text{N}_4$  at the interface in the  $\text{MoO}_{3-x}/\text{g-C}_3\text{N}_4$ . Consequently,  $\text{e}^-$  accumulated in the CB of  $\text{g-C}_3\text{N}_4$  and  $\text{h}^+$  accumulated in the VB of  $\text{MoO}_{3-x}$ .  $\text{H}^+$

was reduced to hydrogen by accumulated electrons at the CB of g-C<sub>3</sub>N<sub>4</sub>, while the TEOA was oxidized by the h<sup>+</sup> accumulated at the VB of MoO<sub>3-x</sub>.

## 4. Conclusions

In this work, we have constructed oxygen-vacancy-rich MoO<sub>3-x</sub>/porous g-C<sub>3</sub>N<sub>4</sub> nanosheets heterojunction by *in situ* growth. The heterojunction photocatalysts under light ( $\lambda = 320\text{--}780\text{ nm}$ ) accelerated photogenerated e<sup>-</sup>-h<sup>+</sup> separation and hydrogen evolution reaction. This method is simple and feasible, which endows g-C<sub>3</sub>N<sub>4</sub> nanosheets with highly porous structure and more active sites, and endows MoO<sub>3-x</sub> with oxygen-vacancy-rich MoO<sub>3-x</sub> and more efficient charge separation, synergistically enhancing the photocatalytic performance. It could be a general method to inorganic semiconductor heterojunction or even multi-junction for photocatalysts.

## Author contributions

H. B. S. conceived the project. Y. F. P. designed and performed the experiments. H. B. S. and Y. F. P. analyzed and interpreted the experimental data. Y. F. P. wrote the paper. H. B. S., Y. W. and Z. L. revised the paper. All authors discussed the results and commented on the manuscript.

## Conflicts of interest

There are no conflicts to declare.

## Acknowledgements

This work was financially supported by Hubei Provincial Natural Science Foundation of China (2020CFA037), and Engineering Research Center of Nano-Geomaterials of Ministry of Education (NGM2019KF023). The authors appreciate the Analytical and Testing Center of China of University of Geosciences (CUG) and the facility support of the Engineering Research Center of Nano-Geomaterials of Ministry of Education, CUG.

## Notes and references

- W. J. Ong, L. L. Tan, Y. H. Ng, S. T. Yong and S. P. Chai, *Chem. Rev.*, 2016, **116**, 7159.
- K. He, J. Xie, X. Luo, J. Wen, S. Ma, X. Li, Y. Fang and X. Zhang, *Chin. J. Catal.*, 2017, **38**, 240–252.
- L. Bi, X. Gao, Z. Ma, L. Zhang and T. Xie, *ChemCatChem*, 2017, **9**, 3779–3785.
- J. Fu, B. Zhu, W. You, M. Jaroniec and J. Yu, *Appl. Catal., B*, 2018, **220**, 148–160.
- R. Daming, K. Sooyeon, F. Mamoru and M. Tetsuro, *Appl. Catal., B*, 2018, **238**, 638–646.
- S. Da Silva Eliana, M. M. N. Moura and M. Neves, *Appl. Catal., B*, 2018, **221**, 56–69.
- Z. Wang, C. Li and K. Domen, *Chem. Soc. Rev.*, 2019, **48**, 2109–2125.
- S. Yang, Y. Gong, J. Zhang, L. Zhan, L. Ma, Z. Fang, R. Vajtai, X. Wang and P. M. Ajayan, *Adv. Mater.*, 2013, **25**, 2452.
- A. Y. Meng, L. Y. Zhang, B. Cheng and J. G. Yu, *Adv. Mater.*, 2019, **31**, 1970294.
- D. W. Wakerley, M. F. Kuehnel, K. L. Orchard, K. H. Ly, T. E. Rosser and E. Reisner, *Nat. Energy*, 2017, **2**, 17021.
- T. Takata, C. S. Pan and K. Domen, *Sci. Technol. Adv. Mater.*, 2015, **16**, 033506.
- C. Liu, D. Kong, P. C. Hsu, H. Yuan, H. W. Lee, Y. Liu, H. Wang, S. Wang, K. Yan, D. Lin, P. A. Maraccini, K. M. Parker, A. B. Boehm and Y. Cui, *Nat. Nanotechnol.*, 2016, **11**, 1098–1104.
- X. C. Wang, K. Maeda, A. Thomas, K. Takanabe, G. Xin, J. M. Carlsson, K. Domen and M. Antonietti, *Nat. Mater.*, 2009, **8**, 76–80.
- J. Liu, Y. Liu, N. Y. Liu, Y. Z. Han, X. Zhang, H. Huang, Y. Lifshitz, S. T. Lee, J. Zhong and Z. H. Kang, *Science*, 2015, **347**, 970–974.
- Z. Hu, L. Yuan, Z. Liu, Z. Shen and J. C. Yu, *Angew. Chem., Int. Ed.*, 2016, **55**, 9580–9585.
- X. Zhu, T. Zhang, Z. Sun, H. Chen, J. Guan, X. Chen, H. Ji, P. Du and S. Yang, *Adv. Mater.*, 2017, **29**, 1605776.
- F. Dai, J. Zai, R. Yi, M. L. Gordin, H. Sohn, S. Chen and D. Wang, *Nat. Commun.*, 2014, **5**, 3605.
- M. David James, *J. Am. Chem. Soc.*, 2014, **36**, 12568–12571.
- G. Liu, T. Wang, H. Zhang, X. Meng, D. Hao, K. Chang, P. Li, T. Kako and J. Ye, *Angew. Chem., Int. Ed.*, 2015, **127**, 13561.
- S. Cao, J. Low, J. Yu and M. Jaroniec, *Adv. Mater.*, 2015, **27**, 2150.
- Z. Yun, L. Lihua, W. Bo and X. Wang, *Angew. Chem., Int. Ed.*, 2015, **54**, 12868–12884.
- J. Zhang, M. Zhang, C. Yang and X. Wang, *Adv. Mater.*, 2014, **26**, 4121–4126.
- P. Niu, L. C. Yin, Y. Q. Yang, G. Liu and H. M. Cheng, *Adv. Mater.*, 2015, **26**, 8046–8052.
- J. Sun, J. Zhang, M. Zhang, M. Antonietti, X. Fu and X. Wang, *Nat. Commun.*, 2012, **3**, 1139.
- D. Zheng, C. Pang and X. Wang, *Chem. Commun.*, 2015, **51**, 17467.
- J. Z. Mao Wu, C. Liu, Y. Gong, R. Wang, B. He and H. Wang, *ChemCatChem*, 2018, **10**, 3069–3077.
- Y. J. Zou, J. W. Shi, D. D. Ma, Z. Y. Fan, L. Lu and C. M. Niu, *Chem. Eng. J.*, 2017, **322**, 435–444.
- M. Gong, W. Fang, Q. Zhao, Y. Li and T. Jiang, *Appl. Catal., B*, 2017, **200**, 601–610.
- D. Kim and K. Yong, *Appl. Catal., B*, 2021, **282**, 119538.
- J. Fu, Q. Xu, J. Low, C. Jiang and J. Yu, *Appl. Catal., B*, 2019, **243**, 556–565.
- Y. J. Zou, J. W. Shi, D. D. Ma, Z. Y. Fan, L. H. Cheng, D. K. Sun, Z. Y. Wang and C. M. Niu, *ChemSusChem*, 2018, **11**, 1187–1197.
- J. W. Shi, Y. j. Zou, L. H. Cheng, D. D. Ma, D. K. Sun, S. M. Mao, L. Sun, C. He and Z. Y. Wang, *Chem. Eng. J.*, 2019, **378**, 122161.
- N. Ding, L. Zhang, H. Zhang, J. Shi, H. Wu, Y. Luo, D. Li and Q. Meng, *Catal. Commun.*, 2017, **100**, 173–177.





- 34 Y. J. Zou, J. W. Shi, L. W. Sun, D. D. Ma, S. M. Mao, Y. X. Lv and Y. H. Cheng, *Chem. Eng. J.*, 2019, **378**, 122192.
- 35 Y. H. Huang, K. Wang, T. Gyo, J. Li, X. Y. Wu and G. K. Zhang, *Appl. Catal., B*, 2020, **277**, 119232.
- 36 J. W. Shi, Y. J. Zou, D. D. Ma, Z. Y. Fan, L. H. Cheng, D. K. Sun, Z. Y. Wang, C. M. Niu and L. Z. Wang, *Nanoscale*, 2018, **10**, 9292–9303.
- 37 J. H. Kim, C. Hyun, H. Kim, J. K. Dash, K. Ihm and G. H. Lee, *Nano Lett.*, 2019, **19**, 8868–8876.
- 38 Y. Chao, P. Zhou, N. Li, J. Lai, Y. Yang, Y. Zhang, Y. Tang, W. Yang, Y. Du, D. Su, Y. Tan and S. Guo, *Adv. Mater.*, 2019, **31**, e1807226.
- 39 H. Zhang, P. Zhang, M. Qiu, J. Dong, Y. Zhang and X. W. D. Lou, *Adv. Mater.*, 2019, **31**, e1804883.
- 40 Y. Xiao, G. Tian, W. Li, Y. Xie, B. Jiang, C. Tian, D. Zhao and H. Fu, *J. Am. Chem. Soc.*, 2019, **141**, 2508–2515.
- 41 X. Liu, B. Wang, M. Liu, S. Liu, W. Chen, L. Gao and X. Li, *Appl. Surf. Sci.*, 2021, **554**, 149617.
- 42 R. Zhang, X. Zhang, S. Liu, J. Tong, F. Kong, N. Sun, X. Han and Y. Zhang, *Mater. Res. Bull.*, 2021, **140**, 111263.
- 43 H. Zhang, L. Yang, P. Zhang, C. Lu, D. Sha, B. Yan, W. He, M. Zhou, W. Zhang, L. Pan and Z. Sun, *Adv. Mater.*, 2021, **33**, 2008447.
- 44 L. Mohrhusen, J. Kräuter, M. Willms and K. Al-Shamery, *J. Phys. Chem. C*, 2019, **123**, 20434–20442.
- 45 M. K. Nowotny, L. R. Sheppard, T. Bak and J. Nowotny, *J. Phys. Chem. C*, 2008, **112**, 5275–5300.
- 46 S. Kohsakovski, P. Pulisova, D. Mitoraj, S. Neubert, J. Biskupek, U. Kaiser, S. Reichenberger, G. Marzun and R. Beranek, *Small Methods*, 2019, **3**, 1800390.
- 47 D. Zhang, Y. Guo and Z. Zhao, *Appl. Catal., B*, 2018, **226**, 1–9.
- 48 H. Yu, R. Shi, Y. Zhao, T. Bian, Y. Zhao, C. Zhou, G. I. N. Waterhouse, L.-Z. Wu, C.-H. Tung and T. Zhang, *Adv. Mater.*, 2017, **29**, 1605148.
- 49 A. Thomas, A. Fischer, F. Goettmann, M. Antonietti, J.-O. Müller, R. Schlögl and J. M. Carlsson, *J. Mater. Chem.*, 2008, **18**, 4893.
- 50 W. Zhang, W. Huang, J. Jin, Y. Gan and S. Zhang, *Appl. Catal., B*, 2021, **292**, 120197.
- 51 H. H. Chen, M. Yang, S. Tao and G. W. Chen, *Appl. Catal., B*, 2017, **209**, 648–656.
- 52 S. Corby, L. Francas, A. Kafizas and J. Durrant, *Chem. Sci.*, 2020, **11**, 2907.
- 53 Y. Geng, D. Chen, N. Li, Q. Xu, H. Li, J. He and J. Lu, *Appl. Catal., B*, 2021, **280**, 119409.

